International Journal of Advanced Materials Chemistry and Physics. Volume 4, Issue 1, (2021) 31-42
http://www.cayley-nielson.com/ijamcp/

Synthesis and Efficient Visible Light Photocatalytic Activity of $FeVO_4/Bi_2MoO_6$ Composite Photocatalysts

Zengmin Wu, Guangjun Yang, Yuanhua Xie*, Min Wang, Tong Zhu*
School of Mechanical Engineering and Automation, Northeastern University, Shenyang, 110004, China
E-mail:*yhxie@mail.neu.edu.cn, tongzhu@mail.neu.edu.cn*

Abstract

Hydrothermal and liquid phase precipitation methods successfully synthesized FeVO4/Bi2MoO6 photocatalysts. Rhodamine B(RhB) assessed the photocatalytic abilities of the composites. The prepared samples were characterized by XRD, SEM, EDS-Mapping, XPS, and UV-vis DRS. When the mole ratio of $FeVO_4$ and Bi_2MoO_6 was 3%, the composite displayed best photocatalytic ability, and the degradation rate of RhB was 64.5%, 27.1% higher than pure Bi_2MoO_6. Recycling experiments presented that the photocatalysts possessed outstanding stability after five-time recycling. The trapping experiments demonstrated that the main active species were h^+ and $\cdot OH$ in the process of RhB degradation. The improved photocatalytic activities were mainly owing to the redshift, the narrower bandgap, and the heterojunctions between $FeVO_4$ and Bi_2MoO_6, which enhances the visible light absorption and inhibits the recombination of the photoinduced electron-hole pairs.

Keywords: $Bi_2MoO_6/FeVO_4$ composite photocatalyst; heterojunction; visible light; rhodamine B.

1. Introduction

There are many kinds of dyestuffs, which bring colors to people's lives and substantial economic benefits.[1] But at the same time, a large amount of dyestuff wastewater is discharged into the environmental water body, resulting in pollution of the natural water body, which endangers human health and aquatic life.[2] Photocatalytic technology, as an advanced oxidation process technology, has sprung up rapidly, which many studies apply to dye degradation.[3-5] The method has many advantages such as low energy consumption, easy operation, no secondary pollution, and complete mineralization of organic matter.[6-8] However, commercial applications of photocatalysts are hampered by factors such as the high composite ratio of photoinduced electron-hole and the low solar energy utilization.[9-11] New and efficient visible-light photocatalyst and full use of solar energy will be the inevitable trend of further practical development of photocatalysis.

Bismuth molybdate (Bi_2MoO_6), a new type of semiconductor photocatalytic material, possesses many advantages, such as a smaller bandgap and better visible-light photocatalytic performance.[12-14] Nevertheless, photoinduced electron-hole recombination limits the broad application of pure Bi_2MoO_6.[15-17] Studies show that the semiconductor composite method can effectively improve the photocatalytic ability of Bi_2MoO_6. Liu et al.[18] have synthesized an Ag_3PO_4/Bi_2MoO_6 composite photocatalyst via the solvothermal method and deposition method, indicating that the combination of Ag_3PO_4 significantly promoted the separation of photoinduced electron-hole and expands the visible light response range, which shows extremely high photocatalytic activity during the degradation of RhB. Jonjana et al.[19] prepared the Bi_2MoO_6 nanosheets with orthogonal phase by the hydrothermal method. It modified the cubic phase

ISSN: 2378-9662, E-ISSN: 2381-5590 / Copyright © 2021 CAYLEY NIELSON PRESS, INC.
May, 2021

AgCl nanoparticles on Bi_2MoO_6 to form the AgCl/Bi_2MoO_6 heterojunction, which inhibited the recombination of photogenerated charge carriers that is highly active and stable in the process of photocatalytic degradation of RhB.

Iron vanadate (FeVO4) is a new functional material with a wavelength of light response above 500 nm and good photocatalytic performance. In this work, based on the hydrothermal synthesis of Bi_2MoO_6, $FeVO_4$ was further synthesized by the liquid precipitation method, and then a new composite photocatalytic material of $FeVO_4$/Bi_2MoO_6 heterojunction was constructed to explore the mechanism by the RhB degradation under visible light illumination.

2. Experimental materials and methods

2.1. Synthesis of photocatalysts

2.1.1. Synthesis of Bi_2MoO_6

Disperse 0.01mol Bi(NO3)3 • 5H2O in 25 mL dilute nitric acid (3mol·L-1) and 5/7mol (NH4)6Mo7O24 • 4H2O in 25ml NaOH solution (6mol·L-1) at room temperature. Then, the two solutions were mixed under magnetic stirring. Then, its pH value was adjusted to 7 by dilute HNO_3 and NaOH solutions. After 30 minutes of continuous magnetic stirring, the mixture was moved to a 100 mL PTFE lined autoclave for sealing and remained at 160℃ for 16 hours. The product is cooled to room temperature by a hydrothermal reaction. Finally, after the samples were collected via suction filtration and washed with DI water and anhydrous ethanol three times separately and then dried at 80℃ for 12 hours, the pure Bi_2MoO_6 powder was obtained.

2.1.2. Synthesis of $FeVO_4$/Bi_2MoO_6 composite catalyst

A certain amount of Bi2MoO6 was dispersed in 40mL of DI water and recorded as liquid A. At room temperature, the raw materials of ferric nitrate and ammonium metavanadate weigh at a molar ratio of 1:1. Then $Fe(NO_3)_3 \cdot 9H_2O$ was dissolved in 10mL of DI water, recorded as liquid B. NH4VO3 was dissolved in 25mL of water and heated to 80° C, magnetically stirred and mixed well to obtain a transparent orange-yellow liquid, recorded as liquid C. According to the molar percentage of $FeVO_4$ and $Bi_2MoO_6$was 1%, 3%, 5%, 10%, and 15%, respectively, the B and C liquids were slowly added dropwise to the A solution correspondingly. Then the pH was adjusted to 2 after stirring and the stirring and continue stirring for 24 hours. After completion of the reaction, the mixture was centrifuged, filtered, and washed several times with absolute ethanol and DI water, then dried at 80 °C for 12h to obtain $FeVO_4$/Bi_2MoO_6 photocatalysts with different compound ratios. Each sample was recorded as: 1%$FeVO_4$/Bi_2MoO_6, 3%$FeVO_4$/Bi_2MoO_6, 5%$FeVO_4$/Bi_2MoO_6, 10%$FeVO_4$/Bi_2MoO_6 and 15%$FeVO_4$/Bi_2MoO_6. For comparison, a $FeVO_4$ sample was obtained by direct precipitation.

2.2. Characteristics of catalysts

The phase composition of the catalyst was detected by a Rigaku D-max-r A-type X-ray diffractometer (XRD) (Cu target Kα ray, test voltage 44kV, current 44 mA, scan range 2θ = 10-70°). The JSM-6700F scanning electron microscope (SEM) equipped with Thermo NORAN Vantage -ESI X-ray energy dispersive spectroscopy (EDS-Mapping) observed the catalyst's microscopic morphology and element distribution. The PHI-5000C ESCA X-type X-ray photoelectron spectroscopy (XPS) was practical to test the binding energy of each element. The use of a Hitachi 1800 UV-visible diffuse reflectance spectrometer (compared to the reference BaSO4) determined the absorption spectrum of the sample.

2.3. Determination of photocatalytic activity

First, Disperse 10 mg photocatalyst into a 50 mL RhB solution (10 mg·L-1) and add a 250 mL beaker. After that, stir the mixture vigorously in the dark for 30 minutes, establishing an adsorption-desorption equilibrium between the catalyst and RhB. The visible light was simulated using a 250 W xenon lamp and a filter placed under the light source that penetrates visible light at a wavelength of λ≥400 nm. During the lighting process, 8 mL of the mixture was removed 10 minutes and centrifuged using a high-speed centrifuge to remove the photocatalyst powders. Finally, the absorbance of the supernatant was measured (λ_{max}=454 nm) on an ultraviolet-visible spectrophotometer, and the decolorization rate of RhB was measured according to the absorbance calculation.

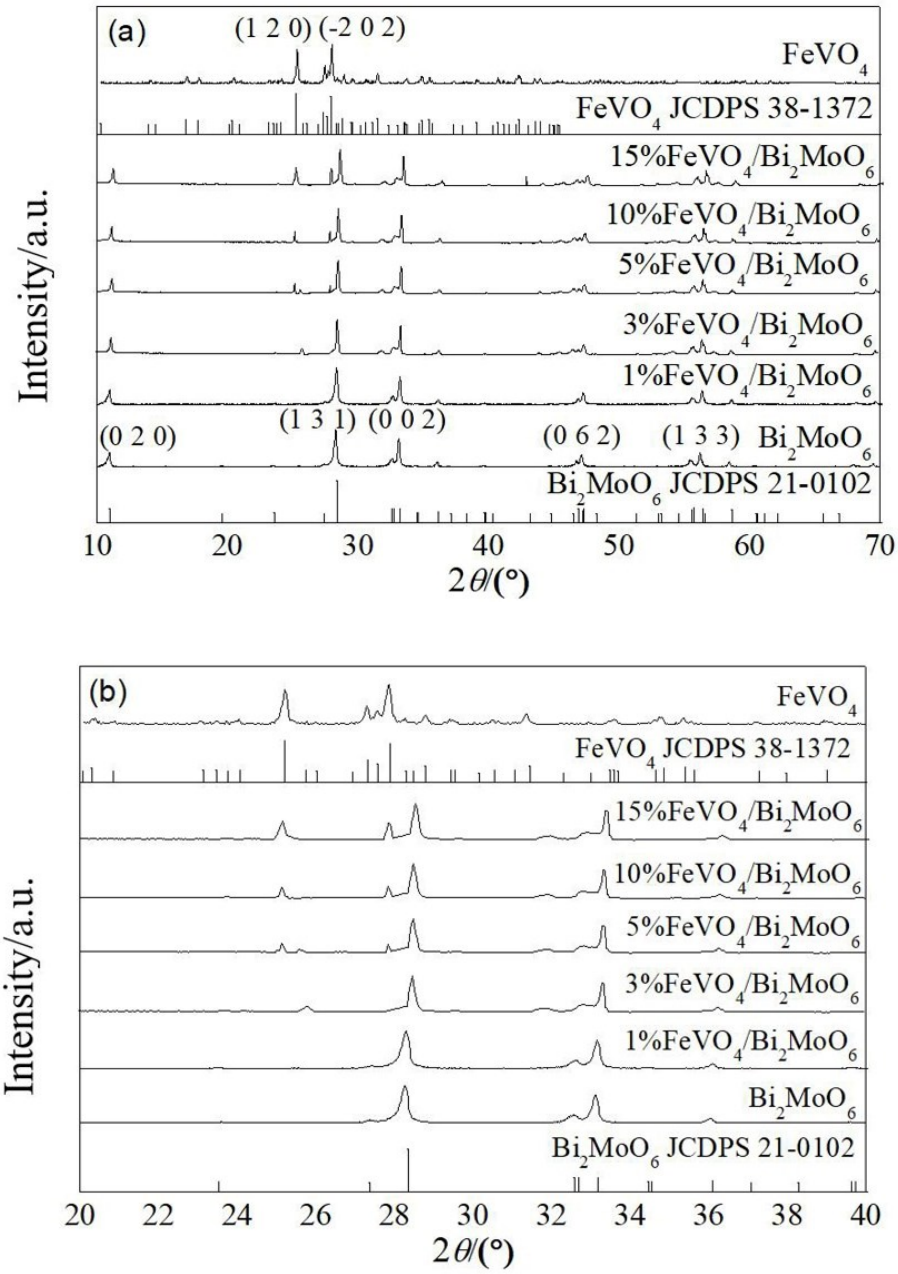

Figure 1. (a) XRD patterns of all samples; (b) enlarged XRD patterns from 20° to 40°

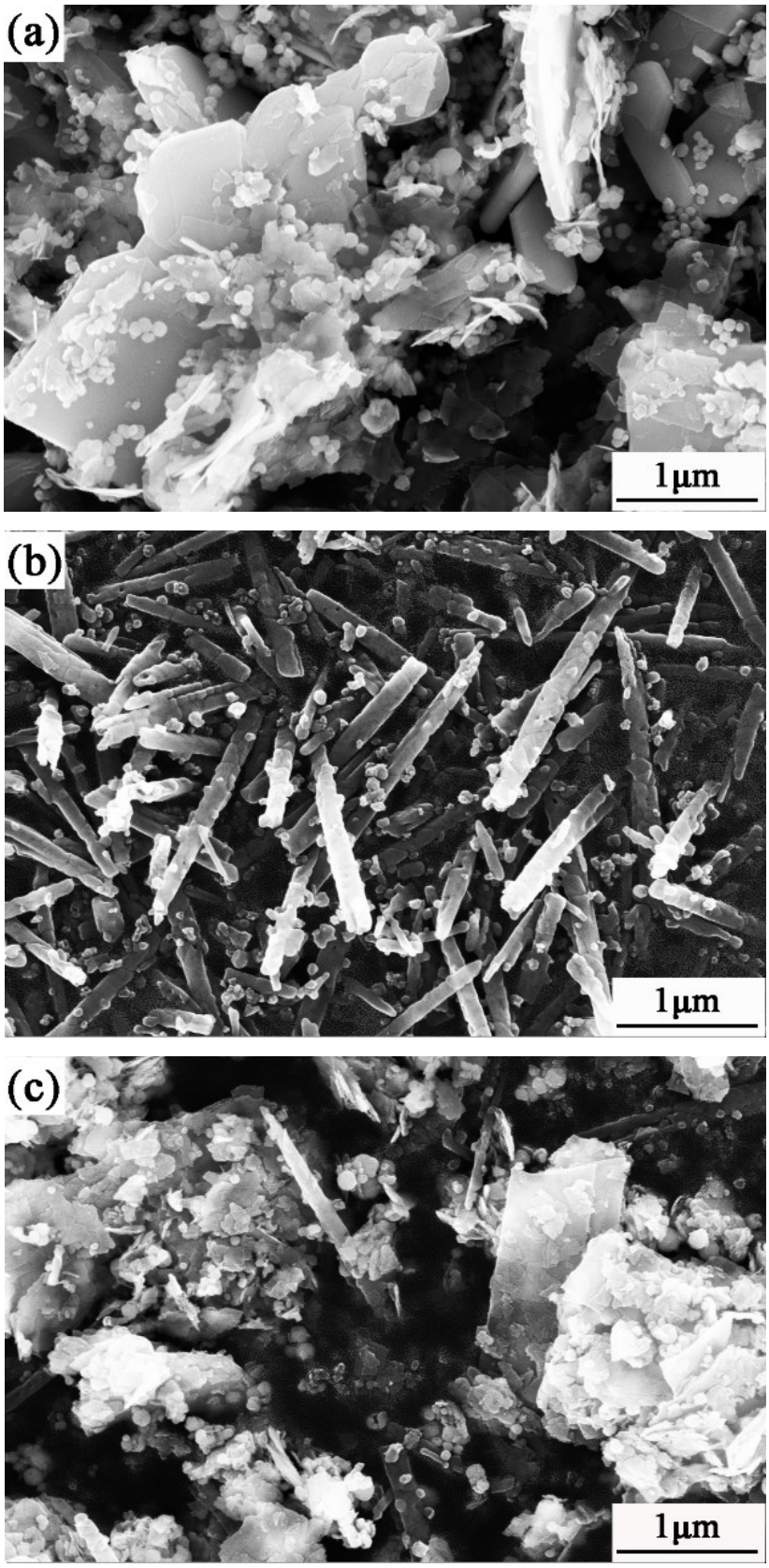

Figure 2. SEM images of (a) Bi_2MoO_6; (b)$FeVO_4$; (c) 3%$FeVO_4$/Bi_2MoO_6

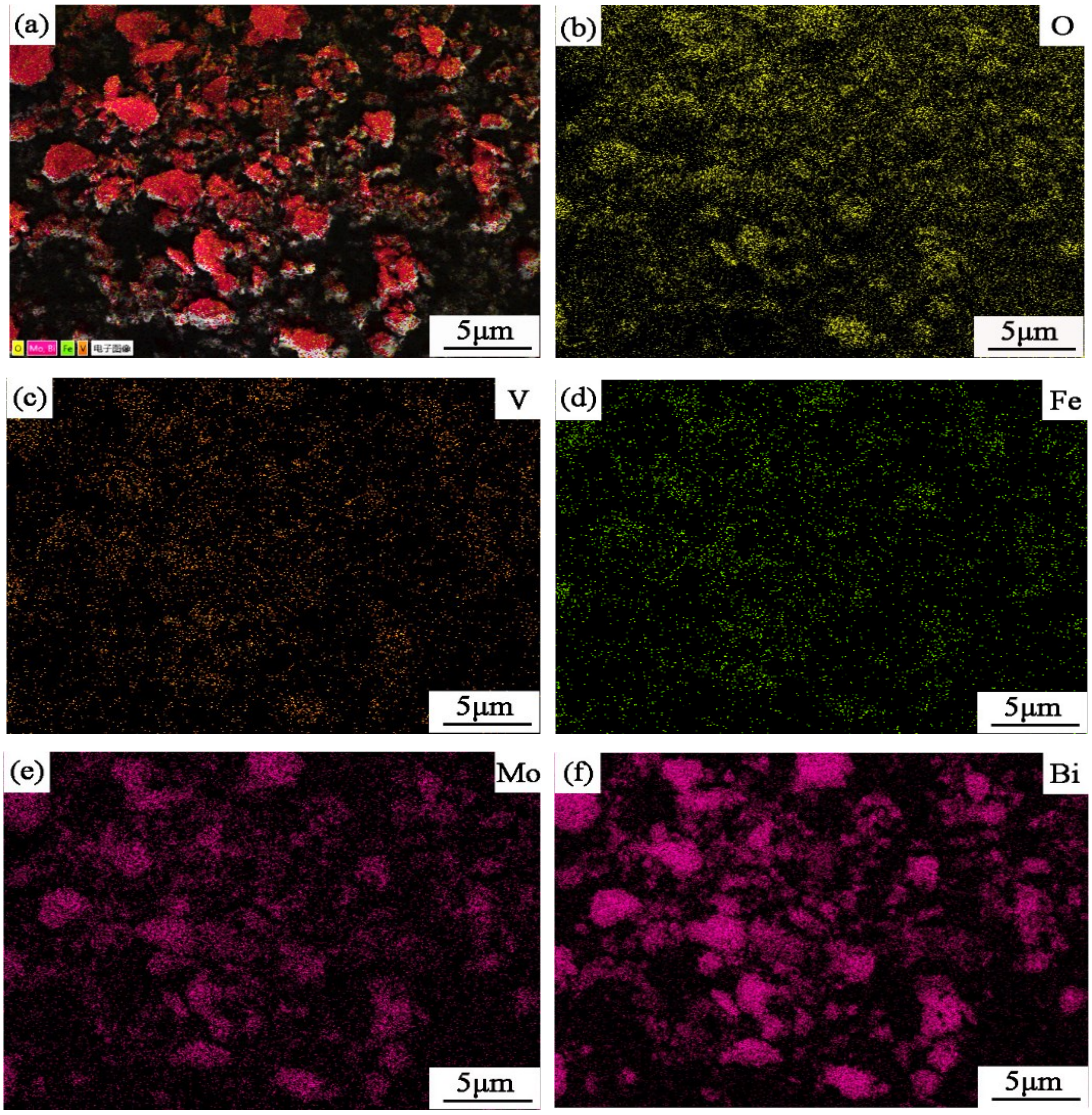

Figure 3. Mapping of 3%$FeVO_4/Bi_2MoO_6$ composite

3. Results and analysis

3.1. XRD analysis

XRD, shown in Figure1, tested the crystalline structures of all samples. The Bi2MoO6 characteristic diffraction peaks are in all samples at approximately 10.9°, 28.3°, 32.6°, 47.2°, 55.6°, indexing to the (0 2 0), (1 3 1), (0 0 2), (0 6 2), and (1 3 3) crystal planes of the Bi2MoO6 standard card (JCPDS 21-0102).[20] This indicates that the hydrothermal synthesis of samples are pure Bi2MoO6 with high purity. The characteristic diffraction peak of the pure $FeVO_4$ sample coincides with the (1 2 0) and (-2 0 2) crystal plane positions in the triclinic phase (JCPDS 71-1592) at 25.0°, 27.7°, indicating that the sample prepared by liquid precipitation method is pure slanted $FeVO_4$.[21] Compared with the XRD peak spectra of five different composite ratio photocatalysts, it can be found that the characteristic peaks of FeVO4 corresponding to 25.0° and 27.7° in the spectrum are gradually obvious with the increase of FeVO4 ratio in the composite samples, indicating that the FeVO4/Bi2MoO6 composite photocatalytic material was successfully prepared by the liquid precipitation method. After loading FeVO4, the strength of the (02) plane weakens slightly, indicating that the combination of FeVO4 and Bi2MoO6 may result in structural

changes rather than mechanical adhesion, which may form a heterojunction structure at their interface. So $FeVO_4$ may mainly grow on this plane and form a heterojunction.[22]

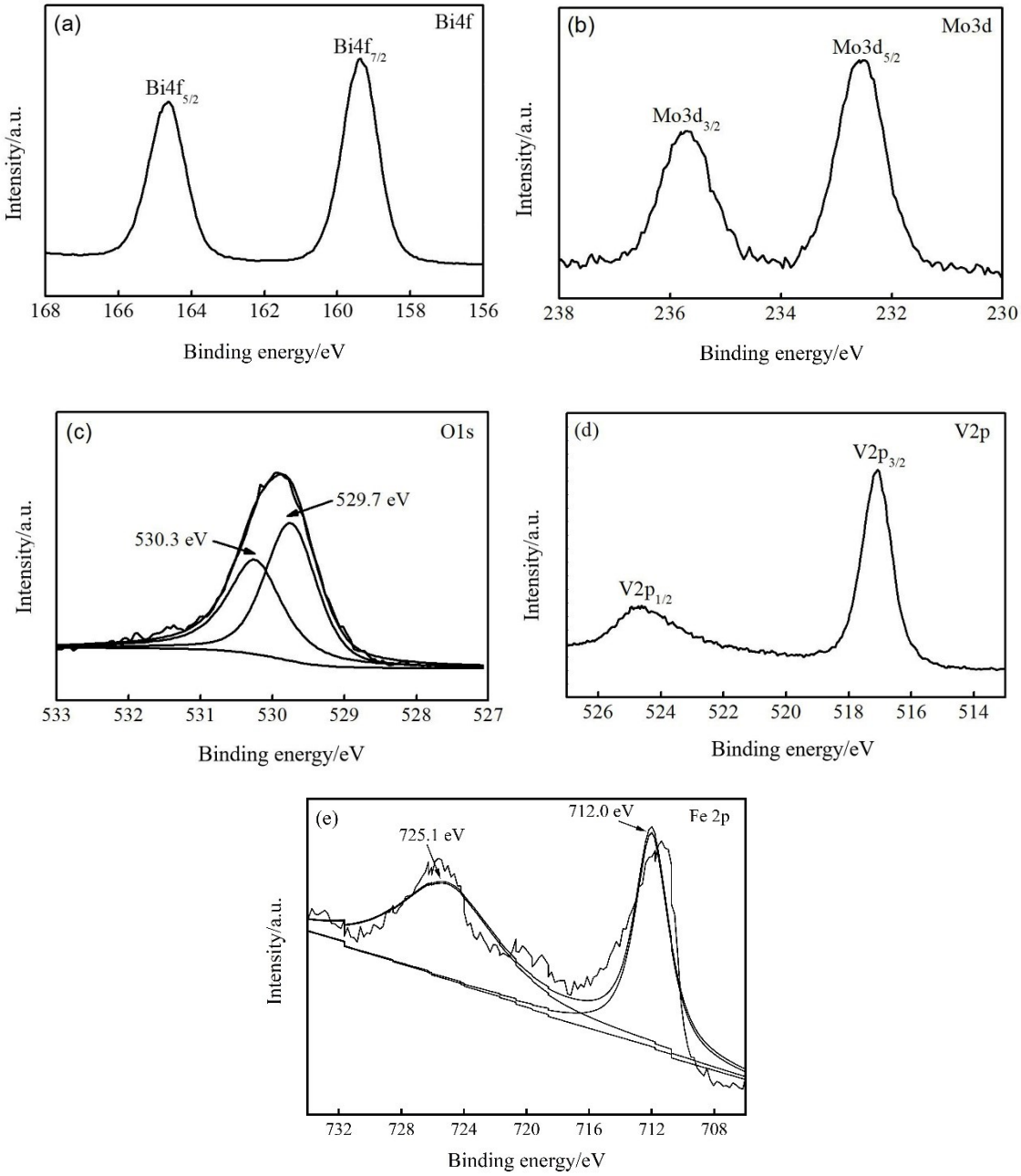

Figure 4. XPS spectra of 3%$FeVO_4$/ Bi_2MoO_6

3.2. SEM and EDS-Mapping analysis

The morphologies of the catalysts were further characterized by SEM images, as shown in Figure 2(a)-(c), respectively. The mapping diagrams of the constituent elements of the composite catalyst are in Figure 3(a)-(f). Figure 2(a) shows that pure Bi_2MoO_6 is a sheet-like structure of different sizes with some small pieces distributed. From Figure 2(b), the pure $FeVO_4$ crystal grains have an elongated rod-like structure with a diameter of about 200 nm. Figure 2(c) shows that the rod-like structure of $FeVO_4$ is embedded among the Bi_2MoO_6 nanosheets, indicating that $FeVO_4$ and Bi_2MoO_6 are effectively compounded in the

3%$FeVO_4/Bi_2MoO_6$ sample. In figure 3(a)-(f), the elements of O, V, Fe, Mo, and Bi are uniformly distributed in the composite photocatalyst demonstrating the uniform recombination of $FeVO_4$ and Bi_2MoO_6.

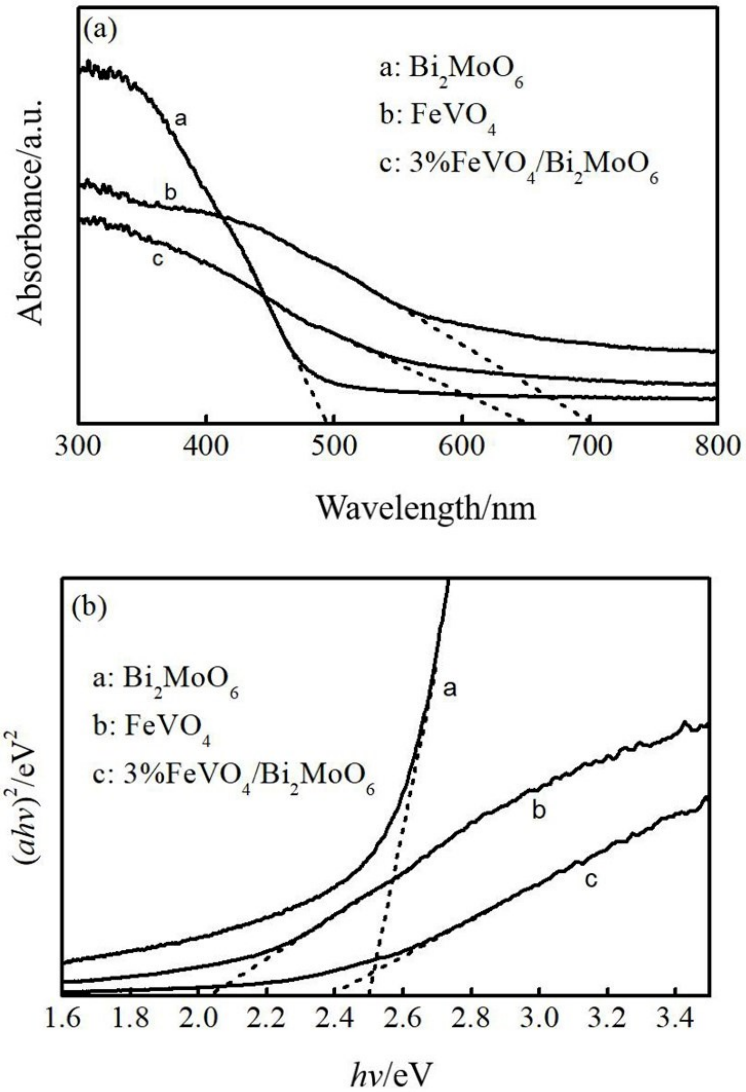

Figure 5. UV-Vis DRS spectra of Bi_2MoO_6, $FeVO_4$ and 3%$FeVO_4/Bi_2MoO_6$

3.3. XPS analysis

To demonstrate the successful preparation of the 3% $FeVO_4/Bi_2MoO_6$ samples, the XPS was utilized to analyze the chemical composition, as shown in Figure 4. From Figure 4(a), the Bi4f high-resolution energy spectrum of the sample shows two distinct characteristic peaks at approximately 164.6eV and 159.4eV, corresponding to $4f_{5/2}$ and $4f_{7/2}$ of Bi^{3+}, which means that Bi exists in the +3 valence state.[23-25] Figure 4 (b) shows that the Mo3d XPS spectrum shows distinct peaks at E_b=232.4eV and 235.4eV, corresponding to $Mo3d_{5/2}$ and $3d_{3/2}$, which indicates Mo exists in the form of Mo^{6+}.[26] In Figure 4(c), the characteristic peak of O1s can be decomposed into two characteristic peaks with binding energies at 529.7 eV and 530.3 eV, assigning to the lattice oxygen of the sample and surface adsorption oxygen.[27] From Figure 4 (d), the high-resolution spectrum of V2p and the characteristic peaks of V2p appearing at 516.9eV and 524.8eV

correspond to $V2p_{1/2}$ and $V2p_{3/2}$, indicating that V in the catalyst exists in the +5 valence state.[28-30] In Figure 4(e), the characteristic peaks of Fe2p appearing at 712.0 eV and 725.1 eV correspond to $Fe2p_{3/2}$ and $Fe2p_{1/2}$, indicating that Fe in the composite system exists in the form of Fe^{3+}.[31-33]

3.4. UV-Vis DRS analysis

The UV-Vis DRS characterization results for three samples of $FeVO_4$, Bi_2MoO_6, and 3%$FeVO_4/Bi_2MoO_6$ are in Figure 5. Figure 5(a) shows that the three samples have strong absorption in the visible light range. The absorption edge of pure Bi_2MoO_6 is about 500 nm, while the absorption edge of $FeVO_4$ is about 700 nm, and the absorption edge of 3% $FeVO_4/Bi_2MoO_6$ sample is about 650 nm. Further, the order of light absorption in the visible light range is $FeVO_4$>3%$FeVO_4/Bi_2MoO_6$>Bi_2MoO_6. From Figure 5(b), the forbidden bandwidths (E_g) of $FeVO_4$, Bi_2MoO_6, and 3%$FeVO_4/Bi_2MoO_6$ are 2.05, 2.5 eV, and 2.4 eV, respectively. The valence band (VB) and the conduction band position (CB) of $FeVO_4$ are 2.53 eV and 0.48 eV, respectively. The VB and the CB of Bi_2MoO_6 are 3.06 eV and 0.56 eV, respectively. The results illustrate that compared with pure Bi2MoO6, the 3% FeVO4/Bi2MoO6 composite photocatalyst shows enhanced absorption of visible light, a significant red-shift phenomenon at the absorption edge and a lower forbidden bandwidth, which is beneficial to improve the photocatalytic activity.

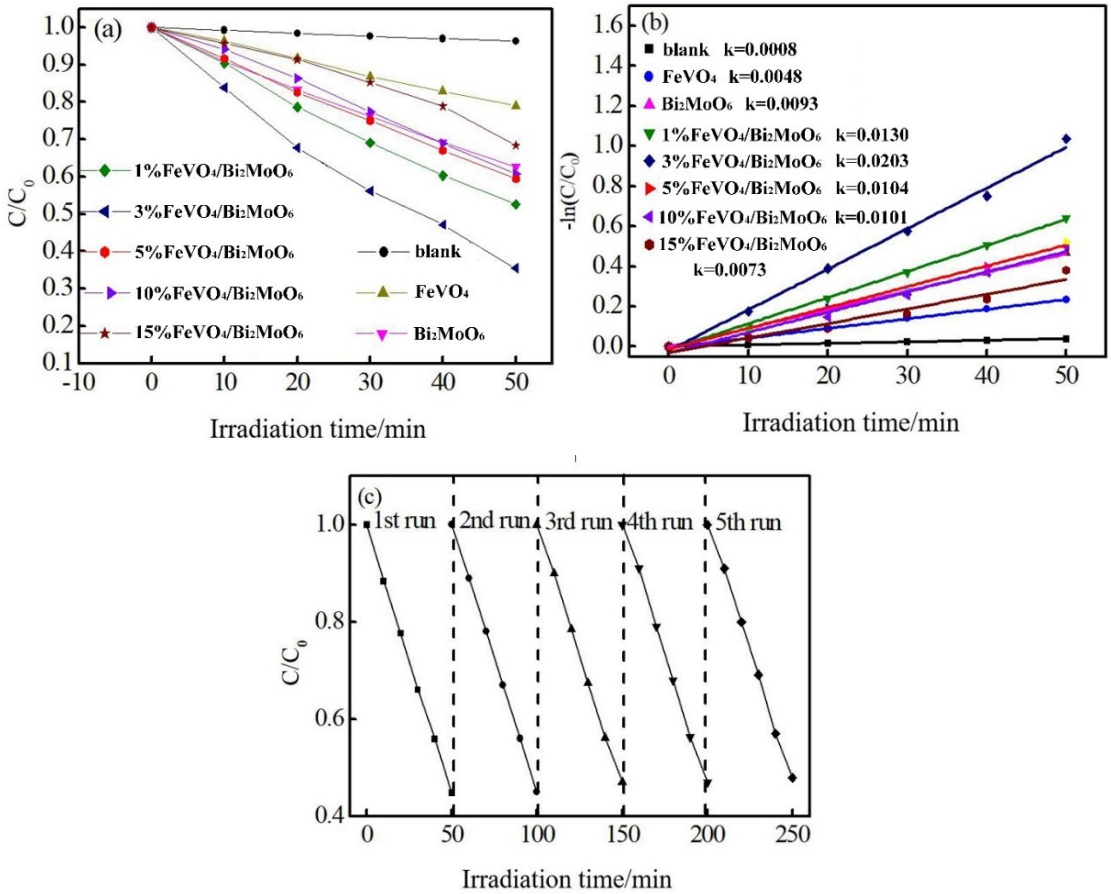

Figure 6. (a) RhB degradation under visible light irradiation of samples (b) -ln(C/C_0) as a function of t of samples (c) Recycling experiments of 3% $FeVO_4/Bi_2MoO_6$ composite

3.5. Photocatalytic activity test and mechanism analysis

3.5.1. Photocatalytic activity test

The test results of photocatalytic ability are shown in Figure 6. From Figure 6(a), the RhB solution hardly degrades after 50 minutes of illumination with no catalyst. The degradation rates of RhB were 21.0% and 37.4% when the pure $FeVO_4$ and Bi_2MoO_6 were in the solution. When the composite ratio of $FeVO_4$ and Bi_2MoO_6 was 1%, 3%, 5%, 10% and 15%, the degradation rates of RhB solution were 47.4%, 64.5%, 39.3%, 40.5% and 27.0%, respectively. When the composite ratio of $FeVO_4$ and Bi_2MoO_6 is low, the photocatalytic activity of the sample enhances with the increase of the composite ratio. The best photocatalytic effect is achieved when the composite ratio of FeVO4 and Bi2MoO6 is 3%, which is about 27.1% higher than that of the single photocatalyst. The photocatalytic activity decreased with further increase of recombination rate, indicating that the optimal composite ratio of $FeVO_4$ and Bi_2MoO_6 is 3%. The first-order reaction kinetics plot of the RhB degradation is shown in Figure 6 (b). The variation of the k value of each sample is: 3%$FeVO_4$/Bi_2MoO_6>1%$FeVO_4$/Bi_2MoO_6>5%$FeVO_4$/Bi_2MoO_6>10%$FeVO_4$/ Bi_2MoO_6>Bi_2MoO_6>15%$FeVO_4$/Bi_2MoO_6>$FeVO_4$. The photocatalytic activity is positively correlated with its first-order reaction rate constant, so the variation of photocatalytic ability is consistent with the change of k value.

At the same time, the stability of 3%$FeVO_4$/Bi_2MoO_6 photocatalyst was investigated by recycling experiments shown in Figure 6 (c). The 3%$FeVO_4$/Bi_2MoO_6 samples showed similar activity in five cycles without apparent deactivation, indicating that the composite catalyst had good stability under visible light irradiation.

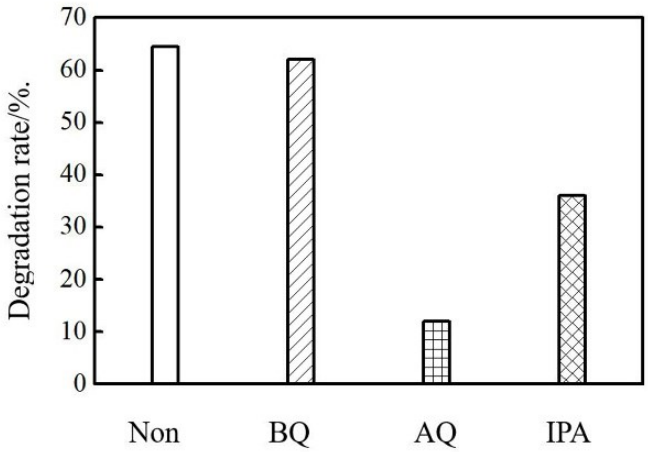

Figure 7. Trapping experiments of 3% $FeVO_4$/ Bi_2MoO_6 composite

3.5.2. Mechanism analysis

In order to investigate the main active oxygen species in the photocatalytic degradation process of the composite system, 3%$FeVO_4$/Bi_2MoO_6 samples were selected for capture experiments. In the experiment, p-benzoquinone (BQ), ammonium oxalate (AO), and isopropanol (IPA) were used as quenchers of superoxide radicals ($\cdot O^{2-}$), holes (h^+) and hydroxyl radicals ($\cdot OH$), respectively.[34] The results are shown in Figure 7. When no sacrificial agent was introduced, the decolorization rate of RhB was 64.5%, and that of BQ, AO, and IPA introduced was 62%, 12%, and 36%, respectively. The introduction of AO had the most obvious effect on the degradation process, and the introduction of IPA followed, but BQ had no

noticeable effect. The results show that the main active species in the degradation process are h^+ and ·OH, and h^+ is more than ·OH.

The mechanism of photocatalytic degradation of RhB by 3% $FeVO_4/Bi_2MoO_6$ composite sample is in Figure 8. Firstly, the VB (+2.53eV) and the CB (+0.48eV) of $FeVO_4$ are higher than those of Bi_2MoO_6 (+3.06eV) and CB (+0.56eV), respectively. They can match well and form the heterojunction structure. Under visible light irradiation, both $FeVO_4$ and Bi_2MoO_6 are stimulated to produce conduction band electrons and valence band holes. Because the CB energy level of Bi_2MoO_6 is more positive than that of $FeVO_4$, electrons are easily conveyed from the CB of $FeVO_4$ to the CB of Bi_2MoO_6. The VB energy level of $FeVO_4$ is more negative than that of Bi_2MoO_6, and the holes are easily conveyed from the VB of Bi_2MoO_6 to the VB of $FeVO_4$ which accelerates the separation of electrons and electron-hole pairs, thereby improves the activity of photocatalysts. Because the CB of $FeVO_4$ and Bi_2MoO_6 is more positive than the electric potential of $O_2/\cdot O^{2-}$, no $\cdot O^{2-}$ is produced during the degradation process. Moreover, the RhB degradation concerns a dye-sensitization mechanism under visible light. RhB (+0.95 eV vs. NHE) is excited to RhB* (−1.42 eV vs. NHE) when irradiated by visible light, then the electrons are conveyed from RhB* into the CB of $FeVO_4$.[35-37] Because the VB of $FeVO_4$ and Bi_2MoO_6 is more positive than the electric potential of H_2O/ ·OH, combining with the capture experiment results, it is obvious that the degradation of RhB is mainly owing to the h^+ hole and the ·OH formed by the further reaction of h^+ with H_2O.

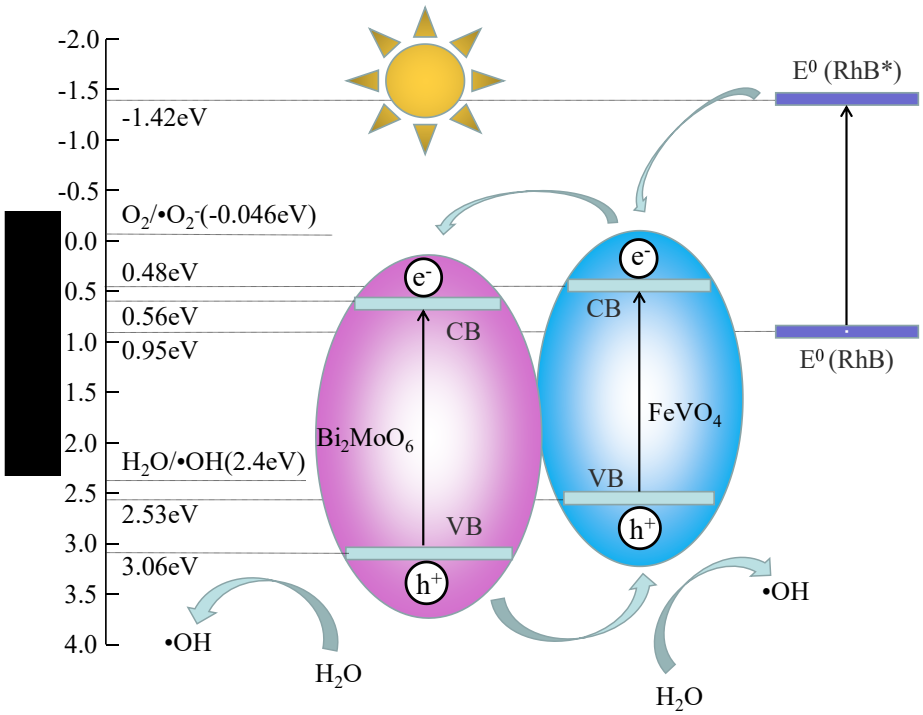

Figure 8. Proposed degradation mechanism of 3% $FeVO_4$/ Bi_2MoO_6 hybrids under visible light irradiation

In summary, the main reasons for the increase of 3%$FeVO_4/Bi_2MoO_6$ composite sample's photocatalytic activities are as follows: firstly, the pure Bi_2MoO_6 prepared in this study has a sheet-like structure, large specific surface area, and many active sites, which improves the photocatalytic activity. The composite of $FeVO_4$ and Bi_2MoO_6, forming a heterojunction structure at the interface between the two

compounds, which effectively promotes the separation of photogenerated electrons and holes, prolongs the carrier lifetime so that increases the activity of the photocatalyst. Furthermore, the recombination of $FeVO_4$ causes a significant redshift in the absorption edge of Bi_2MoO_6, narrows the bandgap and expands the visible light response range, which effectively improves its photocatalytic performance. However, when the composite ratio is more than 3%, the photocatalytic activity decreases with the increase in the composite ratio. Because excessive $FeVO_4$ adheres to the surface of Bi_2MoO_6 and occupies more active sites, which hinders the progress of the photocatalysis reaction and becomes a recombination center of photogenerated electron-holes to reduce the photocatalytic activity of Bi_2MoO_6.

4. Conclusion

(1) The $FeVO_4$/Bi2MoO_6 composite was successfully synthesized by the hydrothermal method and the liquid-phase precipitation method. When $FeVO_4/Bi_2MoO_6$=3% (molar ratio), the effect was the best, and the degradation rate of RhB was 64.5% after 50 minutes of illumination, which was about 27.1% higher than that of pure Bi_2MoO_6. The composite photocatalyst prepared had good repeatability and stability.

(2) XRD, SEM, XPS, UV-vis DRS characterization results reveal that the composite of $FeVO_4$ and Bi_2MoO_6 forms a heterojunction, effectively reducing the photogenerated electron-hole recombination rate, makes the absorption edge of Bi_2MoO_6 redshift, narrows the bandgap and enhances the optical absorption performance. Thereby the photocatalytic activity of Bi_2MoO_6 has been effectively improved.

Acknowledgment

Authors appreciate the financial supporting of the National Natural Science Foundation of China for Youth (No. 21207093).

References

[1] GilPavas, E.; Dobrosz-Gomez I.; Gomez-Garcia M.A.; *Sci. Total Environ.* 2019, 651, 551.

[2] Tsuboy, M.S.; Angeli J.P.; Mantovani M.S.; Knasmüller, S.; Umbuzeiro, G.A.; Ribeiro, L.R.; *Toxicol. In Vitro.* 2017, 21, 1650.

[3] Silva, E.C.; Moraes, M.O.; Brito, W.R.; Passos, R.R.; Brambilla, R.F.; Costa L.P.; Pocrifka, L.A.; *J. Braz. Chem. Soc.* 2020, 31, 1648.

[4] Qin, C.; Liao, H.R.; Rao, F.Y.; Zhong, J.B.; Li, J.Z.; *Solid State Sci.* 2020, 105, 106285.

[5] Liu, H.H.; Yang, C.; Huang, J.; Deng, Z.; Zhong, J.B.; Li, J.Z.; Duan, R.; *Solid State Sci*. 2019, 97, 105989.

[6] Zhang, Y.; Liu, J.; Zhang, Y.; Bi, Y.; *Nano Energy*. 2018, 51, 504.

[7] Teixeira, I.F.; Quiroz, J.; Homsib M.S.; Camargo, H.C.; *J. Braz. Chem. Soc.* 2020, 31, 211.

[8] Rosa M.C.; Nossol B.S.; Nossol E.; Zarbin J.G.; Peralta-Zamora P.G.; *J. Braz. Chem. Soc.* 2017, 28, 582.

[9] Zhang, T.T.; Wang, X.H.; Sun, Z.; Liang, Q.; Zhou, M.; Xu, S.; Li, Z.Y.; Sun, D.Z.; *Solid State Sci*. 2020, 107, 106530.

[10] Li, A.; Peng, Z.J.; Fu, X.L.; *Solid State Sci*. 2020, 106, 106298.

[11] Wang, L.L.; Li, H.; Zhang, S.F.; Long, Y.J.; Li, L.X.; Zheng, Z.G.; Wu, S.L.; Zhou, L.T.; Hei, Y.R.; Luo, L.J.; Jiang, F.Z.; *Solid State Sci*. 2020, 100, 106098.

[12] Wang, M.; You, M.Y.; Guo, P.Y.; Tang, H.Y.; Lv, C.M.; Zhang, Y.; Zhu, T.; Han, J.; *J. Alloys Compd*. 2017, 728, 739.

[13] Lavakusa, B.; Ramesh, A.V.; Srinivasa Rao, N.; Basavaiah, K.; *J. Appl. Chem*. 2017, 10, 11.

[14] Wang, M.; Guo, P.Y.; Yang, G.J.; Chai, T.Y.; Zhu, T.; *Mater. Lett*. 2017, 192, 96.

[15] Zhou, G.L.; Tian, Z.X.; Sun, H.G.; Zhang, J.M.; Zhao, H.Y.; Li, P.; Sun, H.Y.; *J. Phys. Chem. Solids*. 2020, 146, 109577.

[16] Li, Z.Z.; Meng, X.C.; Zhang, Z.S.; *Appl. Surf. Sci*. 2019, 483, 572.

[17] Wang M.; Han J.; Guo, P.Y.; Sun, M.Z.; Zhang, Y.; Zhu. T; You, M.Y.; Lv, C.M.; *J. Phys. Chem. Solids*. 2018, 133, 86.

[18] Du, X.; Wan, J.; Jia, J.; Pan, C.; Hu, X.Y.; Fan, J.; Liu, E.Z.; *Mater. Des*. 2017, 119, 113.

[19] Jonjana S.; Phuruangrat, A.; Thongtem S.; Thongtem, T.; *Mater. Lett.* 2016, 179, 162.

[20] Li, J.L.; Liu, X.J.; Sun, Z.; Pan, L.K.; *J. Colloid Interface Sci.* 2016, 463, 145.

[21] Dutta, D.P.; Ramakrishnan, M.; Roy, M.; Kumar, A.; *J. Photochem. Photobiol. A*. 2017, 335, 102.

[22] Wang, R.X.; Zhu, P.F.; Duan, M.; Xu, J.; Liu, M.; Luo, D.; *J. Alloys Compd*. 2021, 870, 159385.

[23] Ma, T.J.; Wu, J.; Mi, Y.D.; Chen, Q.H.; Ma, D.; Chai, C.; *Sep. Purif. Technol.* 2017, 183, 54.

[24] Wang, M.; Yang, G.J.; You, M.Y.; Xie, Y.H.; Wang, Y.Z.; Han, J.; Zhu, T.; *Trans. Nonferrous Met. Soc. Chi*na. 2017, 27, 2022.

[25] Zhang, M.J.; Lu, J.; Zhu, C.Z.; Xiang, Y.; Xu, L.L.; Chen, T.H.; *Solid State Sci.* 2019, 90, 76.

[26] Cai, J.S.; Huang, J.Y.; Lai, Y.K.; *J. Mater. Chem. A.* 2017, 31, 16412.

[27] Zhang, Z.S.; Zhao, C.X.; Lin, S.L.; Li, H.; Feng, Y.L.; Gao, X.; *Fuel.* 2021, 285, 119171.

[28] Wang M.; Liu, Q.; Che, Y.S.; Zhang, L.F.; Zhang, D.; *J. Alloys Compd.* 2013, 548, 70.

[29] Wang, M.; Guo, P.Y.; Chai, T.Y.; Xie, Y.H.; Han, J.; You, M.Y.; Wang, Y.Z.; Zhu, T.; *J. Alloys Compd.* 2017, 691, 8.

[30] Zheng, Z.X.; Ng, Y.H.; Tang, Y.M.; Li, Y.P.; Chen, W.R.; Wang, J.; Li, X.K.; Li, L.S.; *Chemosphere.* 2021, 263, 128279.

[31] Qiao, J.; Lv, M.Y.; Qu, Z.H.; Zhang, M.; Cui, X.; Wang, D.; Piao, C.C.; Liu, Z.Y.; Wang, J.; Song, Y.T.; *Sci. Total Environ.* 2019, 689, 178.

[32] Long, X.F.; Gao, L.L.; Li, F.; Hu, Y.P.; Wei, S.Q.; Wang, C.L.; Wang, T.; Jin, J.; Ma, J.T.; *Appl. Catal., B* 2019, 257, 117813.

[33] Eshaq, G.; Wang, S.B.; Sun, H.Q.; Sillanpaa, M.; *J. Hazard. Mater.* 2020, 382, 121059.

[34] Wang, Y.; Niu, C.G.; Zhang, L.; Wang, Y.; Zhang, H.; Huang, D.W.; Zhang, X.G.; Wang, L.; Zeng, G.M.; *RSC Adv.* 2016, 6, 10221.

[35] Pan, L.; Zou, J.J.; Wang, S.B.; Huang, Z.F.; Zhang, X.W.; Wang, L.; *Appl. Surf. Sci.* 2013, 268, 252.

[36] Pan, L.; Zou, J.J.; Liu, X.Y.; Liu, X.J.; Wang, S.; Zhang, X.; Wang, L.; *Ind. Eng. Chem. Res.* 2012, 51, 12782.

[37] Mei, J.; Tao, Y.; Gao, C.; Zhu, Q.; Zhang, H.Y.; Yu, J.; Fang, Z.; Xu, H.; Wang, Y.H.; Li, G.S.; *Appl. Catal., B* 2021, 285, 119841.